BACHELOR

AFM assisted nanomanipulation

Muller, C.J.

Award date:
2019

EINDHOVEN UNIVERSITY OF TECHNOLOGY

DEPARTMENT OF APPLIED PHYSICS
PHYSICS OF NANOSTRUCTURES

AFM Assisted Nanomanipulation

Bachelor Final Project

Chris Muller

Supervisors:

H.T. Çiftçi (Hakki Tunç)
dr. O. Kurnosikov (Oleg)

Eindhoven, July 2019

Abstract

Many different SPM methods showed to be very competent in patterning on submicrometric scales, for those especially based on thermal effects often requires external heat sources. In this project, a new approach is introduced which is based on tuning fork-based AFM assisted local thermal surface manipulation using functionalized planar probes (FPP). In this report the sensitivity of this probe is improved, which lead to a quality factor (Q) reaching up to 10^4, which is sufficient to sense even weak interactions such magnetic forces. This setup has also demenstrated resolusions as down to 8.0 ± 0.6 nm of observable surface structures. Besides imaging, also functionalization of this probe is presented, which already showed to be capable of thermomechanical patterning either in ambient or vacuum conditions. In conclusion, this probe showed a high degree of capabilities in operating at high resolution, and is applicable to a wide spectrum of materials.

Preface

During this bachelor final project I have come in contact to a completely new environment on this university, where I learned how to operate in a scientific group and how to function as an independent experimentalist. I really enjoyed having this experience and therefore want to thank everyone at the FNA group. Especially I want to thank my supervisors Tunç and Oleg for guiding me through this project, and I want to thank Tamar for all the support during this project.

Contents

List of Abbreviations

SPM	Scanning Probe Microscopy
STM	Scanning Tunneling Microscopy
AFM	Atomic Force Microscopy
MFM	Magnetic Force Microscopy
vdW	Van der Waals
CM-AFM	Contact Mode AFM
TM-AFM	Tapping Mode AFM
NC-AFM	Non-contact Mode AFM
TF	Tuning Fork
TF-AFM	Tuning Fork based AFM
AM-AFM	Amplitude Modulation based AFM
SPL	Scanning Probe Lithography
AFMEN	AFM-based Electrostatic Nanolithography
FPP	Functionalized Planar Probe

List of Figures

List of Tables

Chapter 1

Introduction

In modern science the constant urge to operate on smaller scales have led to several breakthroughs. One of the most famous examples is the challenge to keep up with Moore's law, but also in chemical and biological fields it is essential to understand the physics from submicron to nanometer scales. Biologic microscope techniques are already developed such that biological samples such as DNA, proteins, membranes or other cells are able to be investigated on submicrometric scales [1–3]. It is just a matter of time before these techniques are not only able to characterize, but also to manipulate features on the smallest bioscales.

Progress in this field is impossible to achieve without the proper use of characterization mechanisms. In the last decades a lot of progress lead to several microscope techniques, capable of visualizing structures on the atomic scale. Several of these techniques, such as scanning probe microscopy (SPM), also showed to be very suitable for patterning and other surface manipulation processes. In the last years SPM has been widely applied as nanolithography tool and still shows a great potential in further functionalization features, but at the same time still a lot of challenges have to be solved.

One of the challenges in nano-patterning is to reduce the dependency on external factors, such heat sources or applied magnetic fields, which are often used in many of the current state of the art SPM techniques. These external applied parameters, such as heat, often affect large parts of the sample, which can cause damages, changed nature of the materials or irreversible deformations. This is the reason for introducing functionalized probes, obtaining a setup which is less dependent on external parameters. However, prior techniques have not been able to produce local modification only with self-induced probes so far.

In this project the implementation and utilization of **functionalized planar probes** will be discussed. These probes are able to produce controllable thermal influence, well-confined at any selected position. First, the microscopic capabilities of this probe will be examined by implementing it in in an atomic force microscope and optimizing it's resolution by examining the implementation in a vacuum setup. Next, the probe will be tested on it's functionality under these conditions, by performing thermal surface manipulations.

Chapter 2

Background

In 1981 the scanning tunneling microscope (STM) was developed in as an alternative for existing optical and electron microscopes [4]. The technique was based on a scanning probe carrying an electronic tunneling current, resulting in very high resolution imaging. The development of STM was a truly scientific revolution because this technique was the first to be able to visualize individual atoms. STM would turn out to be the first out of many surface-investigating scanning techniques bundled together as **scanning probe microscopy (SPM)**.

These high resolution SPM techniques are suitable to functionalize to perform surface modifications on submicrometric scales, that reach beyond the resolution of visible light. However, the majority of these techniques still has not shown all it's potential, due to complexity or fragility of the probes for exploiting thermal effects, chemical interactions and voltage-induced processes in different patterning operations.

2.1 Atomic Force Microscopy

Atomic force microscopy (AFM) is a SPM technique monitoring forces between tip and sample and using this to construct a topographic profile of the sample surface in high resolution [5], as shown in fig. 2.1. Due to it's flexibility and ease in use, AFM is a very popular tool in modern nanocharacterization but also showed to have a lot of potential in the field of nanomanipulation. In contrast to STM, AFM is not restricted to operate on conductive samples, and thus is more capable in efficiently investigating non-conductive samples such as polymers or biological tissue. In comparison to AFM, STM needs a very complex setup in order to achieve electron tunnel currents. The usage of AFM demands a much less complex setup which therefore has a higher ease of use.

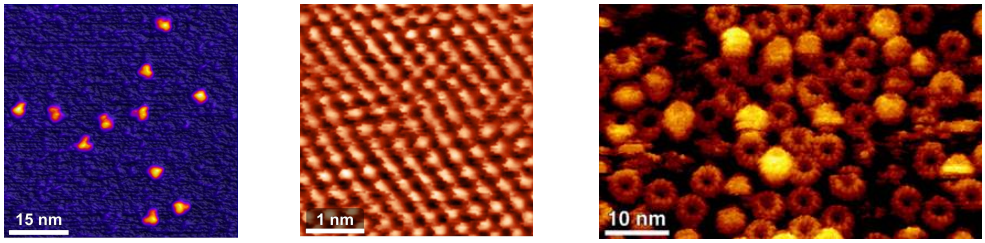

(a) Antibody molecules (b) HOPG (c) Proteins

Figure 2.1: Several high-resolution AFM results. Retrieved from [6]

2.1.1 AFM working principle

Conventional AFM setups consist of a silicon based **cantilever** to which a probe is attached. When this probe is positioned at small heights above the sample surface, the cantilever will deflect as a result of certain forces. This deflection is detected by a laser, as visualized in fig. 2.2a. The laser is focused on the cantilever, of which the light will reflect the light at a certain angle. The reflected laser light then will be collected by a quadruple diode detector. Different deflections of the cantilever will result in different reflection angles, from which the tip-sample distance can be determined. This information will be analyzed by a feedback controller (often a PID or phase locked loop controller), which ensures that the tip-sample distance remains constant and the tip will not crash into any surface feature.

Techniques involving a Si-cantilever and laser detection are the most common used types of AFM, but there are several setups developed based on other mechanisms. In figure 2.2b the principle of **tuning fork** based AFM (TF-AFM) is shown, which has specific advantages for our approach. The theory behind cantilever based AFM will be discussed in this section briefly. In section 2.1.2 the specific properties of tuning forks will be discussed.

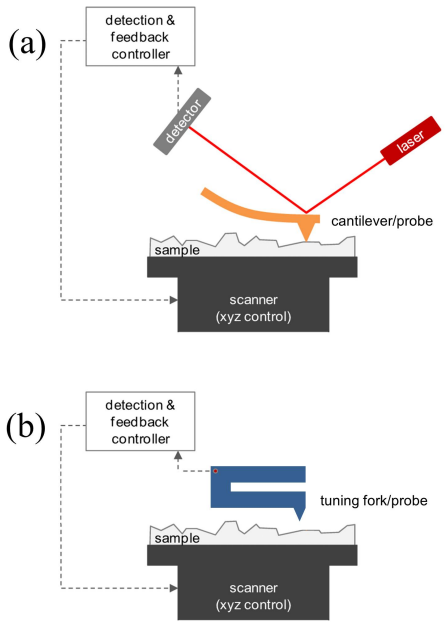

Figure 2.2: Operating principles of cantilever based (a) and tuning fork based (b) AFM.

The tip-sample interaction force strongly depends on the distance between tip and sample, which will be referred to as D. To obtain information about the topographic structure of a certain sample, it is essential that D is in the range of 1 to 10 nm, where the dominating force acting on the tip is caused by the *Van der Waals* (vdW) interaction [7, 8]. As shown in table 2.1 also other forces will act on the tip, but in the range of 1 to 10 nm these are significantly small in comparison to vdW forces and can therefore be neglected. At other heights different forces will be dominant, which can tell something about other material properties. For instance, at $D \sim 100$ nm magnetic effects will be dominant in the system, which can be measured to obtain information about magnetic properties of the material. This method is referred to as magnetic force microscopy (MFM).

Table 2.1: Dominating forces on different distances from the sample

$D \downarrow$	1000 nm	Electrostatic forces
	100 nm	Magnetic forces
	10 nm	Van der Waals forces
	1 nm	Chemical forces
	0.1 nm	Exchange forces

In the region of interest for AFM ($1 < D < 10$ nm) the total exerted force on the tip can be described by a **Lennard Jones potential** [9]. A Lennard Jones potential (V_{LJ}) is a mathematical model describing the attraction and repulsion between two atoms or particles.

The Lennard Jones potential V_{LJ} can mathematically be expressed as

$$V_{\mathrm{LJ}}(r) = 4\epsilon \left[\left(\frac{\sigma}{r}\right)^{12} - \left(\frac{\sigma}{r}\right)^{6} \right], \tag{2.1}$$

with ϵ the depth of the potential well, σ the distance at which $V(r)$ equals zero and r the tip-sample distance. $V_{\mathrm{LJ}}(r)$ is plotted in fig. 2.3, from which easily can be seen that at small r both particles will strongly repel each other. Here the repulsive surface forces are dominant, corresponding with the first term in eqn. 2.1. At increasing r the repulsion force will decrease with a factor r^{-12}. For $r > \sigma$ the attractive vdW force will dominant, corresponding with the second term in eqn. 2.1. At $4 \approx 4$ Å (1 ångström = 0.1 nm = 10^{-10} m) the potential has a minimum. For larger r the curve of $V(r)$ will now show the long-range vdW dependency, $V(r) \propto r^{-6}$.

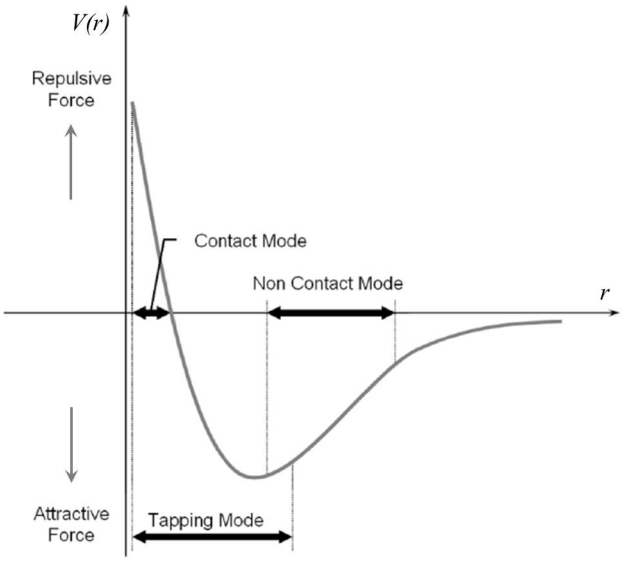

Figure 2.3: Typical AFM force-distance curve, showing regions of repulsive and attractive forces on the tip. In this figure r_m is the distance at which the potential reaches it's minimum.

AFM Operation modes

An AFM can operate in different modes, each having certain advantages and disadvantages. The conventional mode to operate an AFM is using **contact mode** AFM (CM-AFM). In CM-AFM the tip is "dragged" over the sample surface as shown in fig. 2.4a. The deflection of the cantilever can be measured to construct the topography of the sample. One of the disadvantages of using CM-AFM is the fact that the dragging of the probe over the surface can cause serious damages to the sample, especially to soft materials. **Tapping mode** AFM (TM-AFM) was developed to avoid these surface damages by using a vibrating cantilever 'tapping' the surface [10,11], as shown in fig. 2.4b. This reduced the possible damages to surface, and often used to investigate samples in liquid, due to low resistance and tip contamination [12]. For both CM- and TM-AFM it is required that the probe makes physical contact with the surface. For strong probes this does not have to be an issue, but for several probes this contact can cause damages to the probe. This problem could be resolved by using the **non-contact mode** AFM (NC-AFM). In this mode the probe is oscillating at high frequency above the sample surface as visualized in 2.4c.

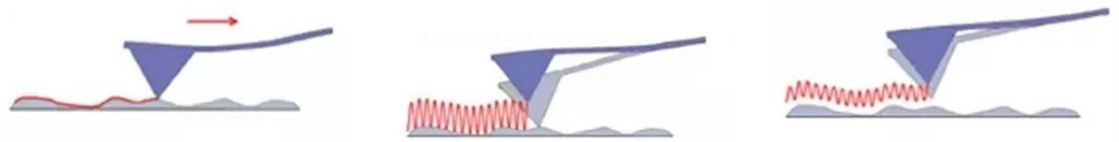

(a) Contact mode AFM (b) Tapping mode AFM (c) Non-contact mode AFM

Figure 2.4: AFM operation modes. Reprinted from [13]

Because of the unique specialised probes used in this project (which will be further elaborated in section 3.1), NC-AFM is the most suitable operation mode in this project, as it does not require any physical contact between tip and sample. In this way possible damages to the tip are prevented. In the following section the physical background of this operation mode is elaborated further.

Non-contact mode AFM

Non-contact mode AFM (NC-AFM) is based on the principle of frequency modulation (FM), making use of the frequency gradient of the tip [14, 15]. The result is that the probe does not longer have to physically touch the sample, which prevents damages to both the tip and the sample.

When the tip-sample distance is large, the probe is able to oscillate at it's resonance frequency ω_0. At this point, the cantilever potential $V(z)$ has only one contribution to this potential, described by a harmonic oscillator. When the probe is brought close to the surface (but not making contact), the probe will experience a force gradient $\partial F/\partial z$, causing the cantilever's spring constant to modified to $k' \rightarrow k + \partial F/\partial z$. As $f_0 = (1/2\pi)\sqrt{k/m}$ [16], this will result in frequency shift $\Delta f = f - f_0$, with f the frequency under influence of a force gradient. In this system $\partial F/\partial z$ is described by the Lennard-Jones potential V_{LJ}, which will alter the total effective potential $V(r)$. Between $3.5 < z < 7$ Å it slightly lowers $V(z)$ and for $z < 3.5$ Å it creates the limit $V(z \downarrow 0) \rightarrow \infty$. All these potentials are presented in fig. 2.5a. This asymmetric potential can be analyzed by a Fourier Transform, resulting in the already stated frequency difference Δf, plotted in 2.5b. This can be used as a calibration for the tip-sample distance D.

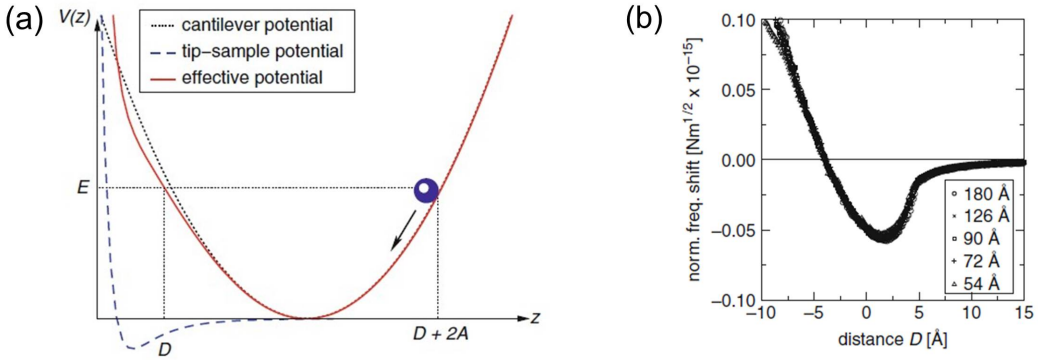

Figure 2.5: Effective potential of an NC-AFM probe from contributions of the cantilever potential and the tip-sample interactions in (a). In (b) the resulting frequency shift Δf which is normalized for different amplitudes. Reprinted from [14]

2.1.2 Tuning fork-based AFM

Due to the high capability of Si cantilever based AFM setups of obtaining high resolution images, Si-cantilever AFM has become a very popular characterization tool in many scientific applications. Unfortunately, the use of a optical laser in this setup can create several problems. One of the challenges is to investigate light sensitive samples using laser light detection. The use of a laser can also have result in other complications, as the laser is able to damage to the cantilever. Several studies showed that quartz **tuning forks** can serve as a suitable alternative for Si cantilevers [16].

Quartz tuning forks were developed as a tool for frequency control and are now widely used in applications such as clocks and watches. The working principle of a tuning fork (TF) is based on the oscillation of the two prongs sketched in fig. 2.6b. This oscillation will be driven at the forks resonance frequency f_0, which is typically in the range from 10 kHz to 600 kHz. Due to the piezoelectric properties of quartz, an oscillation of the prongs will cause a piezoelectric current. This current is a direct measure of the amplitude of the oscillation, which together with the discussed frequency shift Δf in NC-AFM this information can be used to define the tip-sample distance D. One of the major advantages of this technique is the fact that the detection mechanism does not require a laser anymore and is based on purely electric signals. This allows the tuning fork to operate in different conditions, such as for instance in liquid-based operations.

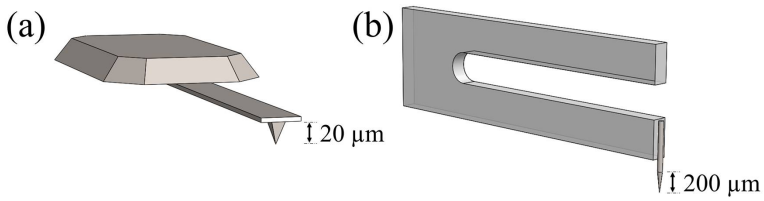

Figure 2.6: Setups for cantilever based AFM (a) and tuning fork based AFM (b).

Tuning fork based AFM setups do not involve a laser-based detection mechanism, which makes TF-AFM a suitable alternative to investigate light sensitive samples. Instead, the detection mechanism in quartz tuning fork force sensors are based on the piezolectric properties of quartz. A quartz TF is able to vibrate itself and detect the probe deformation if an electrical voltage is applied to it. This deformation will unleash a small measurable piezo current. The amplitude of this current is a direct measure of the degree deformation. Deformation of the tuning fork can be interpreted as a counter oscillation of both of the prongs. To achieve this, the tuning fork can be excited both electrically or mechanically.

When a tuning fork is driven electrically, the inverse piezoelectric effect is used by applying a voltage across the TF to induce a deformation of the tuning fork. When this voltage is an AC voltage resonating with the fork's resonance frequency, the TF will oscillate at a maximum amplitude. The current through the TF can be used to define this amplitude, which is a measure for the experienced force by the tuning fork.

Another possibility is the use of an external piezoelectric element attached to the TF, which excited the tuning fork mechanically at resonance. Due to the piezo-electric effect the fork will generate a piezo current, which will be a measure for the generated amplitude of the fork, that is directly linked to the experienced force.

Quality factor (Q)

For both Si-cantilever based and tuning fork-based AFM setups, frequency based oscillation discussed in section 2.1.1 are impossible without a proper frequency characterization. To obtain high resolution images, the aim is to minimize damping of the oscillation. This damping can be interpreted as dissipation of energy, which can described by the dimensionless quality factor (Q) [17]. Q is expressed as the ratio between the total energy in the system and the average energy loss in one cycle:

$$Q = 2\pi \times \frac{\text{energy stored}}{\text{energy loss per cycle}} = 2\pi \frac{E}{\Delta E}. \tag{2.2}$$

The Q factor originates from the damping term in the equation of motion for a damped harmonic oscillator, which is given by

$$\frac{\mathrm{d}^2 z}{\mathrm{d}t^2} + 2\zeta\omega_0 \frac{\mathrm{d}z}{\mathrm{d}t} + \omega_0^2 z = 0, \tag{2.3}$$

with z the vertical displacement of the tip, $\omega_0 = \sqrt{k/m}$ the resonance frequency of either the cantilever or the tuning fork and ζ the damping ratio. Eq. 2.3 can be solved for z using an ansatz technique resulting in

$$z(t) = Ce^{st}, \quad s \equiv -\omega_0 \left(\zeta \pm i\sqrt{1-\zeta^2}\right), \tag{2.4}$$

where C and s both are complex constants. The value of the damping ratio ζ now determines whether the oscillation is undamped ($\zeta = 0$), underdamped ($0 \leq \zeta < 1$), critically damped ($\zeta = 1$) or overdamped ($\zeta > 1$). The Q factor is directly related to ζ as [18]

$$Q = \frac{1}{2\zeta}, \tag{2.5}$$

from which easily follows that during AFM measurements should be aimed for maximized Q factors in order to suppress damping in the system. This can experimentally be achieved by performing a frequency sweep and minimizing the bandwidth of the resonance frequency peak [19, 20]

$$Q = \frac{\omega_0}{\Delta\omega_{\mathrm{FWHM}}}, \tag{2.6}$$

with $\Delta\omega_{\mathrm{FWHM}}$ the full width at half maximum. This ratio defines the bandwidth of an oscillator. Oscillators with small bandwidth (fig. 2.7a) will have a high Q factor and therefore will have well defined eigenfrequency. A small frequency perturbation therefore will be easily observable in such systems. For low Q oscillators with large bandwidths (fig. 2.7b), a small perturbation will be much harder to observe, which negatively affect the sensitivity of the setup.

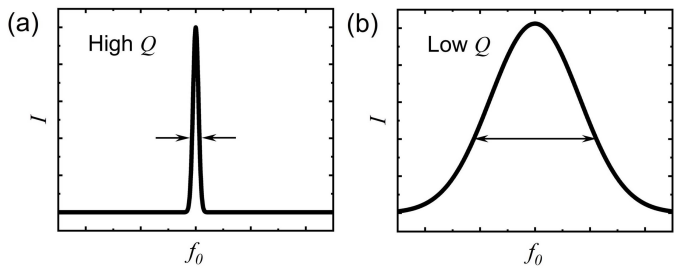

Figure 2.7: Two spectra showing the difference between an oscillator with a small bandwidth and high Q in (a), and with a large bandwidth and low Q in (b).

2.1.3 AFM Sensitivity

As stated in the previous section, the sensitivity of the AFM is for a major part dependent on the Q factor. This logically follows from figures 2.7(a and b) in combination with theory discussed in section 2.1.1. As soon as the probe is brought close to the surface, under the influence of the Van der Waals the effective potential will change resulting in a frequency shift $\Delta f = f - f_0$ between the long range resonance frequency f_0 and the resonance frequency close to the surface f. This frequency shift is visualized in fig. 2.8 for oscillating systems with high (a) and low (b) Q factors.

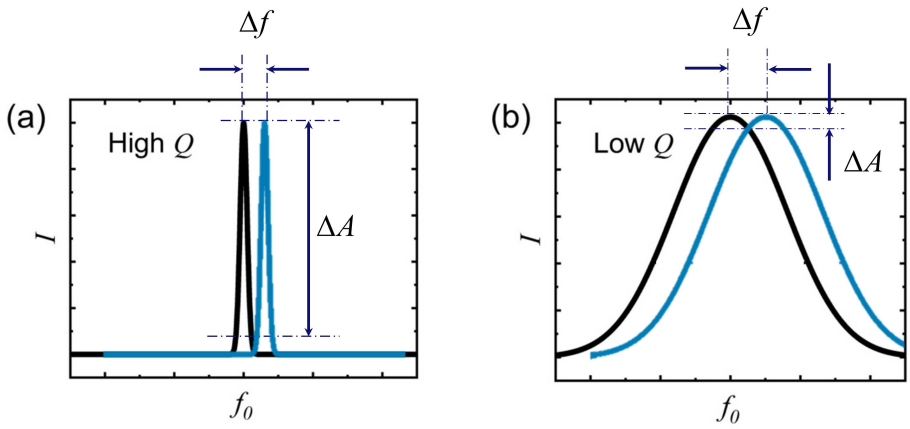

Figure 2.8: The difference between high (a) and low (b) Q value oscillators on the sensitivity of the system, described by the measurable amplitude ΔA after a frequency shift Δf.

As soon as a frequency shift is caused by surface forces, an amplitude difference ΔA will be observable, as indicated in both figures. For high Q value systems (fig. 2.8a), the overlap between both peaks is small, and both peaks are therefore easy to distinguish from each other. For low Q value systems (fig. 2.8b) the overlap between the peaks is much higher and therefore the amplitude difference is much smaller. In tuning fork systems, this amplitude difference ΔA is directly measured by the released piezo current, so in order to obtain optimized sensitivity it is preferable to have ΔA (and thus Q) as high as possible.

Phase Shift

This amplitude modulation (AM) based technique is very suitable for a lot of SPM techniques, however in many other techniques not this amplitude, but a phase shift $\Delta\phi$ in the oscillation is used to characterize the sensitivity of the setup. For example for friction measurements, $\Delta\phi$ is used to compare materials as different materials will have different interactions resulting in different shifts in phase. Despite that this project is based on AM-AFM, the theory behind phase differences can provide a well-based insight in the resolution differences between cantilever and TF-based AFM.

Maganov showed in his study that the phase angles in cantilever based AFM depends on several parameters such as the quality factor Q and the cantilever's stiffness k. For force gradients that are small comparing to Q/k, the phase difference between a free oscillating cantilever and the interacting cantilever can be approached by [10]

$$\Delta\phi \approx \frac{Q}{k}\frac{\partial F}{\partial z}, \tag{2.7}$$

with $\Delta\phi = \phi_0 - \phi$ as the difference of the phase of the the free cantilever ϕ_0 and the phase of an interacting cantilever ϕ. The discussed frequency shift can be described by a phase shift $\Delta\phi$ The possible resolution which can be achieved using AFM depends on several parameters, of which the discussed

Conventional silicon-based cantilevers with $Q_c \approx 200$ and $k_c \approx 3\,\mathrm{N\,m^{-1}}$ have proven to achieve resolutions of several ångströms. In order to reach these resolution using tuning fork techniques, the same phase shift should be satisfied in eq. 2.7 and therefore the following relation should be satisfied:

$$\frac{Q_{\mathrm{TF}}}{k_{\mathrm{TF}}} \stackrel{!}{=} \frac{Q_{\mathrm{c}}}{k_{\mathrm{c}}}. \tag{2.8}$$

The stiffness of a tuning fork is a property which has been investigated in several studies, which led to an expression for the TF stiffness given by [21]

$$k_{\mathrm{TF}} = \frac{Ewt^3}{4L^3}, \tag{2.9}$$

with E as Young's modulus and w, t and L respectively the width, thickness and length of the tuning fork. In order to obtain a phase shift as large as possible, it is desired to minimize the TF stiffness. This is the reason why the majority of tuning forks have relatively long prongs in comparison to their width and thickness. Although this reduces the stiffness, the value of k_{TF} will always be around two order higher than the stiffness of cantilevers. This is due to the strong material properties of quartz in comparison the the soft silicon. To compensate for this, the Q factor of the used tuning fork should be (according to eq. 2.9) obey to

$$Q_{\mathrm{TF}} \simeq 10^4, \tag{2.10}$$

in order to be able to reach the same resolutions. Several TF-based measurements in vacuum achieved Q factors that meet this requirement [16, 21], since all the ambient noise caused by air particles is cancelled. That is why the use of vacuum systems will be thoroughly investigated in this project.

2.2 Atomic force microscope-assisted applications

SPM methods has not only shown to be very competent in characterization on the nanometer scales, but emerged as a popular tool for surface manipulation, as known as scanning probe lithography (SPL) [22–25]. SPL techniques have proven to be very flexible patterning tools, and depending on the tip-sample interaction the SPL can be driven by mechanical, thermal, chemical and electrostatic mechanisms. Ragerding the use of our approach in thermomechanical writing now we take a look at prior studies in this field.

2.2.1 AFM-assisted thermal surface modification

The usage of **thermal** SPL systems showed some very interesting properties, as it is wider applicable on target samples that do not have to meet certain criteria as conductivity. This makes lithography tools based on thermal advection very popular in polymer researches, but also in biological fields. Together with earlier established techniques such as thermal-mechanical writing, the SPL formed the basis for several industrial prototypes such as **AFMEN** (based on the electrostatic lithography) and **Millipede** (based on thermomechanical writing).

AFMEN

In 2003 Lyuksyutov et al. introduced a nanolithography technique which was based on manipulation of the dielectric properties of a thin polymer film combined with external Joule heating [26–28]. This technique named AFM-based electrostatic nanolithography (AFMEN) makes use mass transport in initially uniform, planar films. At first the complete film is heated above the glass transition temperature T_g. At this temperature the polymer will show capillary instabilities which submitted to a strong (10^8-10^9 $\mathrm{V\,m^{-1}}$) external applied electric field, will interact with electrostatic and/or Van der Waals attractions by the AFM tip, which results in formation of raised structures as visualized in fig. 2.9.

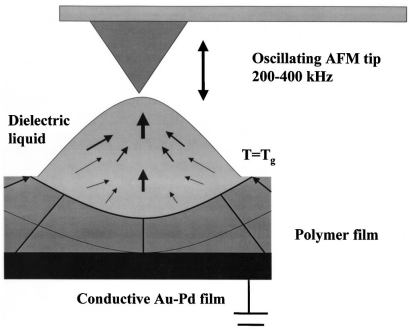

Figure 2.9: Working principle of AFMEN. Reprinted from [26]

Although AFMEN is able to form structures in many polymers with different physical-chemical properties, AFMEN still shows limitations. In order to obtain a dielectric film it essential to heat up the entire sample, which for certain materials irreversibly can damage the sample. Besides that, another criterion is that the target sample must be able to reach the glass temperate T_g is a viscous state, in order to be sensitive to vdW forces. This limitation has the consequence that only a few materials are suitable for measurements using AFMEN.

Millipede

Another thermal nanolithography tool called the Millipede [29, 30], was designed as new tool in data storage, uses a different approach of thermal surface manipulation. The Millipede system is built up out of an 2D array of AFM cantilevers, as visualized in fig. 2.10. The densest array consists of 32×32 (1024) cantilevers, which leads to a storage density of 60-75 Gb/cm^2. All cantilevers in this array are separately able to heat up and press on the surface. Writing has been accomplished by thermal-mechanical lithography techniques. To write data, all heated tips in the array are pressed upon the surface. Tips that are set to write are heated up to relative high temperatures (about 400°C) to locally melt the surface. To optimize the melting process, more force is applied to the tips to penetrate the sample and leave a hole as soon as all tips are withdrawn. These holes serve as bits and can be designed to store data.

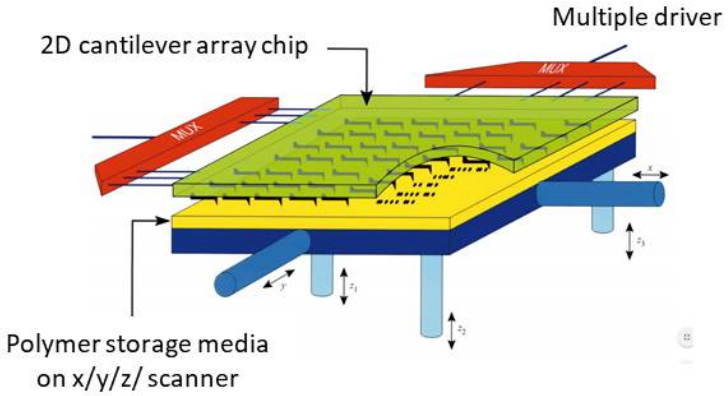

Figure 2.10: Schematic presentation of the Millipede setup. Reprinted from [29]

The usage of Millipede shows some great potential, but when this technique is used in characterization methods like SPM, it shows some problems. The tips used in Millipede are set to physically touch and penetrate the sample, which would affect the SPM scan quality. When tips are exposed to these forces, it will be extremely hard to maintain a setup which can perform reproducible measurements.

Both AFMEN and Millipede are technologies that are well-integrated in modern nanopatterning, but as discussed both techniques still have their limitations. However, combining these techniques can result in a very promising, wide applicable, setup, which is the basis for the **new approach** in this project, that will be discussed in the next chapter.

Chapter 3

New Approach

Both AFMEN and Millipede showed great potential in thermal AFM-assisted patterning, but both systems also encountered certain limitations. AFMEN requires that the whole sample is heated which can cause irreversible changes to the nature of the sample. Systems operating with Millipede use probes which physically touch the sample surface, risking damages to both the sample and the tip. In this project a new thermal nanolithography tool is designed and used, based on the principles of both AFMEN and Millipede.

When the heating technique in Millipede is used in AFMEN-AFM tips, the local non-contact surface manipulation in AFMEN is maintained, but without the need of external heat sources. This implies that only the targeted spot is exposed to heat and the rest of the sample remains untouched. This principle is visualized in fig. 3.1, with a heated tip that is able to locally melt the surface (fig. 3.1a). Due to the capillary instabilities, this melted part of the surface will now be sensitive to Van der Waals forces, causing the matter to rise towards the tip (fig. 3.1b). As long as the temperature at the tip-end is well-controlled, the tip withdraws fast enough due to feedback control from this rising surface and possible tip-crashes are prevented. As soon as heating is turned of, the matter stops rising and will quickly solidify leaving a formed structure as in fig. 3.1c.

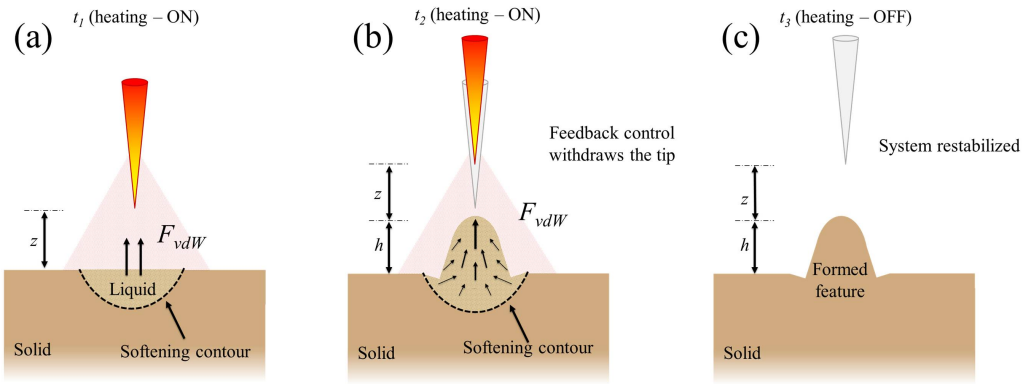

Figure 3.1: A local surface is heated (a) which is then softened, making it sensitive to Van der Waals forces causing it to rise (b), and stabilize after the system is cooled down (c).

3.1 Functionalized planar probes

To create a setup based on this principle, it is crucial to gain full control over the temperature control at the tip-end without any loss of scanning quality. Conventional AFM tips are produced from silicone and attached to a Si cantilever (fig. 3.2a) or metallic wires glued on a quartz tuning fork (fig. 3.2b). But as soon as these tips are implemented in a setup for thermal patterning, it turns out that both tips fail in temperatue control at tthe tip end. When probes in cantilever based setups are heated, due to heat dissipation the cantilever will heat up as well, which has a negative effect on the laser-based detection. The feedback control will be affected which can lead to tip-crashes. The use of cantilever-based AFM setups is therefore rather complicated in combination with thermal surface manipulation. A solution to this problem could be the use of a tuning fork based AFM, since the scanning procedure can be performed by just the upper prong while thermal fluctuations will occur at the end of the lower prong. Thermal properties will therefore not affect the oscillation of the tuning fork. Although, the use of a needle-shaped probe as in fig. 3.2b did not result in full temperature control at the tip end [16].

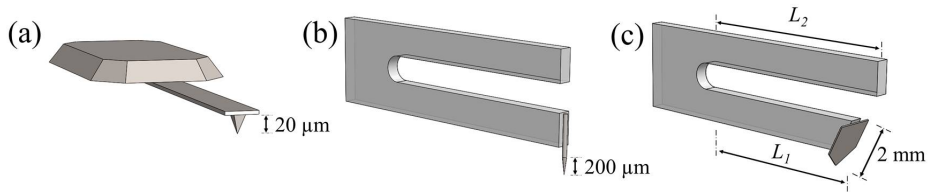

Figure 3.2: Conventional AFM tips on a Si cantilever (a) and attached to a tuning fork (b), and the new approach using an oversize FPP (c).

To overcome these problems, we developed the **functionalized planar probe** (FPP). In contrast to the needle-like conventional probes in fig. 3.2(a and b), the FPP (fig. 3.2c) has a large tailored surface in order of a few mm^2 which can be relatively easily adapted and functionalized. The FPP already showed in an earlier study to be capable of imaging on atomic levels in STM [31], and therefore has a lot of potential in the combination of high imaging AFM and thermal surface modification.

The FPP is constructed in such as way that has a very sharp conductive tip-end, at which a 40 µm wide "microbridge" is formed (fig. 3.3a). When a voltage is applied over both sides of this bridge, a confinement of electrical current will take place at the tip-end. This confinement will locally cause a very high current density which results in a temperature increase of the tip-end (fig. 3.3b). This temperature can be regulated by controlling the magnitude of the applied current.

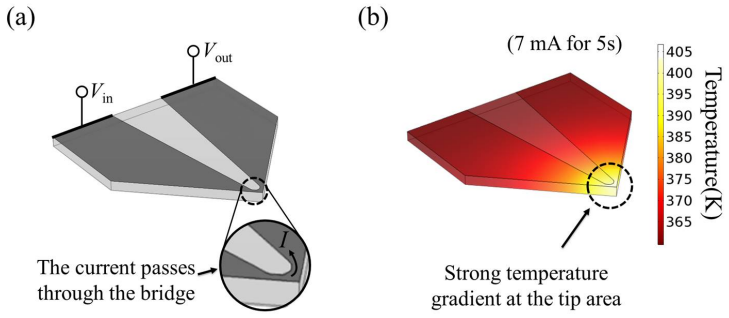

Figure 3.3: A tailored FPP containing a nanobridge at the tip end. An applied voltage will cause a current confinement, causing a increase of current density at the tip-end (a), which results in a local heating of the tip-end (b).

As the FPP is controllable in regulating the temperature at the tip-end, the FPP is been found suitable for the AFM-assisted thermal surface nanomanipulation as discussed in the begin of the chapter. In fig. 3.4 this method is visualized again, in combination with the working principle of the FPP.

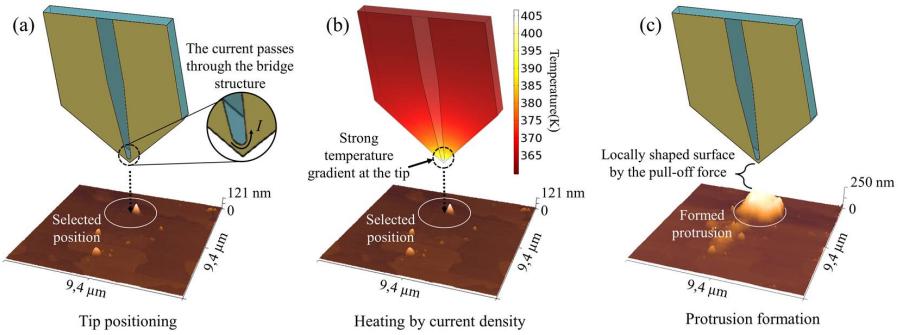

Figure 3.4: The working principle of AFM-assisted nanomanipulation using the FPP. The tip will be brought close to the sample surface (a), will drive a current over the nanobridge to produce heat at the tip-end (b) and will therefore form a surface feature by vdW forces (c).

In this project structural changes of the surface morphology of **paraffin wax** will be investigated. The advantage of using paraffin wax is the fact that it is a well known material with well determined phase-transition parameters. The glass transition (T_g), cold crystallization peak (T_{cc}) and melting peak (T_m) temperatures at respectively 309 K, 318.7 K and 330.6 K [32]. In this stage the main aim is to examine the reliability of the functionalized probes will be investigated, using paraffin wax. However, when this functionality has been proven, this approach can be applicable to a broad range of other materials.

In order to accurately reach these temperatures, it is essential that the applied current over the nanobridge is well regulated. This current will cause a local temperature gradient at the surface, resulting in the formation a surface features as discussed in section 2.2.1. To estimate appropriate values of the applied current I and exposed time t, a model will be used, which will be discussed in the methodology chapter.

3.2 FPP Implentation in TF-AFM

The implementation of the FPP in AFM systems is preferred by the use of a tuning fork over a cantilever, as the tuning fork has a stiffness which is several orders larger than the cantilever. Therefore the tuning fork is able to deal with the large load of the FPP, which is hard to achieve using cantilever-based systems. Another advantage of tuning forks is that the scan en patterning processes can be electrically separated completely. The upper prong can be used for monitoring the oscillating while the lower prong contains wires to the FPP, controlling the the thermal processes, as shown in fig. 3.5. In this way thermal advections will never affect the oscillation. Therefore the implementation of FPP in AFM setups in this project will be based completely on TF-AFM.

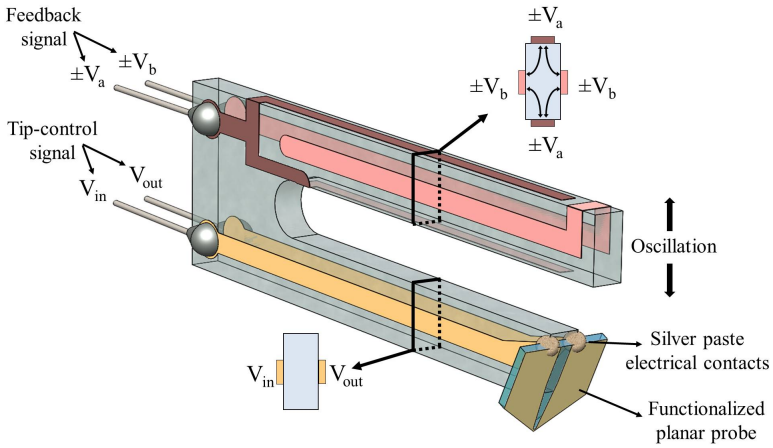

Figure 3.5: Total setup containing a FPP attached to a TF, of which the upper prong contains a piezoelectric circuit to control the oscillation, and the lower prong is wired to the FPP.

Although the use of a tuning fork is more suitable than using a cantilever, the system still needs to be optimized. The attachment of a probe to the tuning fork causes an asymmetry in the system, which will negatively affect the sensitivity of the tuning fork. [33–35]. The sensitivity of the discussed setup can be described by the minimum force it is able to measure. This minimum detection force able to achieve using TF-sensors can be expressed in terms of the stiffness k, eigenfrequency f_0 and the quality factor Q of the tuning fork as [36]

$$F_{\text{min}} \propto \sqrt{\frac{k}{f_0 Q}}. \tag{3.1}$$

After attachment of the FPP on the TF (1) the resonant frequency f_0 will decrease due to the extra mass involved and (2), the oscillation will be much more damped due to the asymmetry resulting in a decrease of Q. Implementation of these adaptations in eq. 3.1 results in a higher F_{min} and thus in lower sensitivity. As the Q factor is mainly responsible for this change in sensitivity, in this project the aim will be to reach Q factors as high as possible. In conventional TF-AFM setups (fig. 3.2b) this problem was resolved by minimizing the dimensions of the attached probe in order to reduce the extra load on the lower prong. However, it is practically impossible to reach similar dimensions using a large scaled FPP. This challenge has to be overcome before the FPP is able to perform high resolution measurements.

Chapter 4

Methodology

In order to obtain a functioning setup, the first focus is to fabricate the FPP in such a way it meets all requirements to operate as discussed in section 3.1. The next step will involve the implementation of the FPP in an conventional AFM setup. This setup will be able to perform measurements in both ambient and vacuum conditions.

4.1 FPP Fabrication

In order to succesfully fabricate the FPP, certain challenges have to be resolved. In order to optimize the probes scanning and patterning resolution, the size of the probe's tip has to be minimized. It is also essential that the FPP is attached to the tuning fork in such a way that the optimal sensitivity can be reached. The fabrication process of the FPP is discussed by Çiftçi in his paper [37], where the process is split up into four stages: cleaving, tailoring, rebalancing and functionalization.

The FPP is produced using a top-down approach, starting from a 100 µm thick silica-glass slab. This slab is coated by a thin metallic layer, which consist of Ta(3)/Pt(50)/Al(2), to obtain a good conductance. By double cleaving, introduced by Sihaan et al in [31], it has been proven that sharp tips can be achieved with a tip-end of 10 nm. The tip then is tailored using electroerosion and focussed ion beam (FIB) in order to obtain a microbridge at the tip-end.

Now as the FPP is ready to be implemented, the FPP is bonded to a quartz tuning fork (of resonance frequency $f_0 = 32.611 \pm 0.001$ kHz) using a strong light cure adhesive drop (LOCTITE, 4305). To obtain electrical access to the tip, silver paste is applied on the contacts (Holland Shielding Systems Bv, 3980 Shieldokit). However, the attachment of the FPP to a tuning fork will induce an instability, as discussed in section 3.2. To resolve this, the lower prong is shortened in order to compensate for the extra mass of the FPP, as visualized in fig. 4.1.

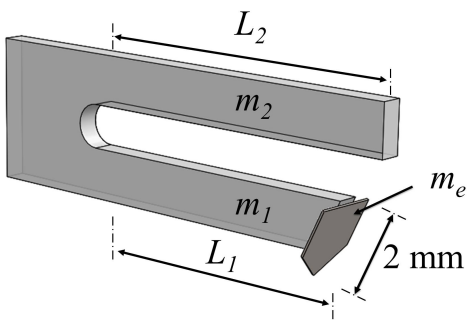

Figure 4.1: Adapted TF with different prong lengths L_1, L_2 to compensate for the mass difference caused by m_{em}.

When the lower and upper prong have respectively lengths L_1, L_2 and masses m_1, m_2 and the FPP carries a mass m_e, the mass difference between the two prongs can be defined as

$$\Delta m = (m_1 + m_e) - m_2. \tag{4.1}$$

Theoretical calculations performed by Rychen et al. in [33] predict that the highest Q value is obtained at $\Delta m = 0$, which will be tested experimentally by measuring Q factors at different values of Δm. The optimal value for Δm will be used in the setup.

COMSOL Model

The functionalization of the FPP is based on the sent current trough the microbridge, and in order to sufficiently heat the tip-end without burning the tip, it is essential to apply appriopriate currents. In order to estimate these properties, Çiftçi modelled the time-dependent heat dissipation using COMSOL. COMSOL models are based on finite element analysis together with advanced simulations software, which is widely used to model for instance electrical, mechanical, fluid, and chemical applications. To obtain physical parameters, the model is run at different values for the current I, of which two results are shown in fig. 4.2a. According to this figure, it takes only several milliseconds to reach the melting temperature of paraffin in ambient conditions. When the paraffin sample is heated for several seconds, a surface formation will be achieved under influence of the Van der Waals force, as discussed in the previous chapter. This formation is shown in fig. 4.2c and 4.2e.

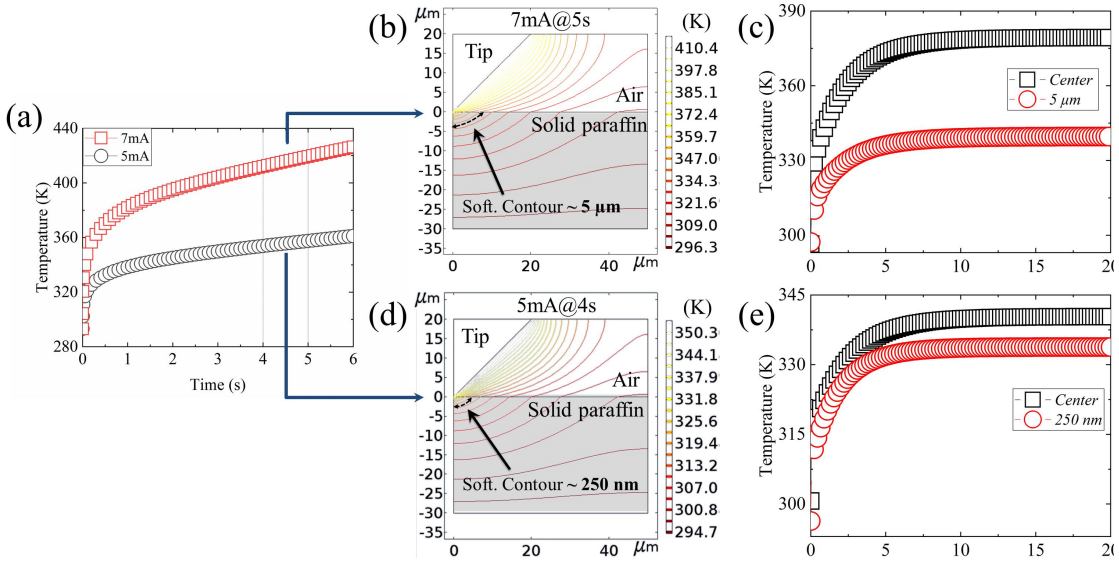

Figure 4.2: Results from the COMSOL model, the time dependent tip temperature for $I = 5$ mA in black and 7 mA in red (a), the contour maps of the heat dissipation for both currents (b, d) and the time dependent heat characteristics of the paraffin surface at the center (black) and at the softening contour (red) for both currents (c, e).

4.2 Experimental setup

The tuning fork is implemented the experimental setup as shown in fig. 4.2. The tuning fork (fig. 4.2d) is attached to a adapter on which all electronic contacts are established (fig. 4.2c). This adapter consists of a Mini USB Type C plug, which can be connected to the AFM head (fig. 4.2a) which is part of the complete AFM setup in fig. 4.4 (NT-MDET NTEGRA, SNLG113USB model). The sample to be investigated is positioned right under this AFM head. The used NTEGRA AFM setup has been equiped with a vacuum chamber, as visualized in fig. 4.4. Using an external vacuum pump, it is able to reach pressures of 0.007 mbar. This enables the AFM to perform measurements in vacuum conditions, which can positively affect the sensitivity of the AFM as discussed in section 2.1.3.

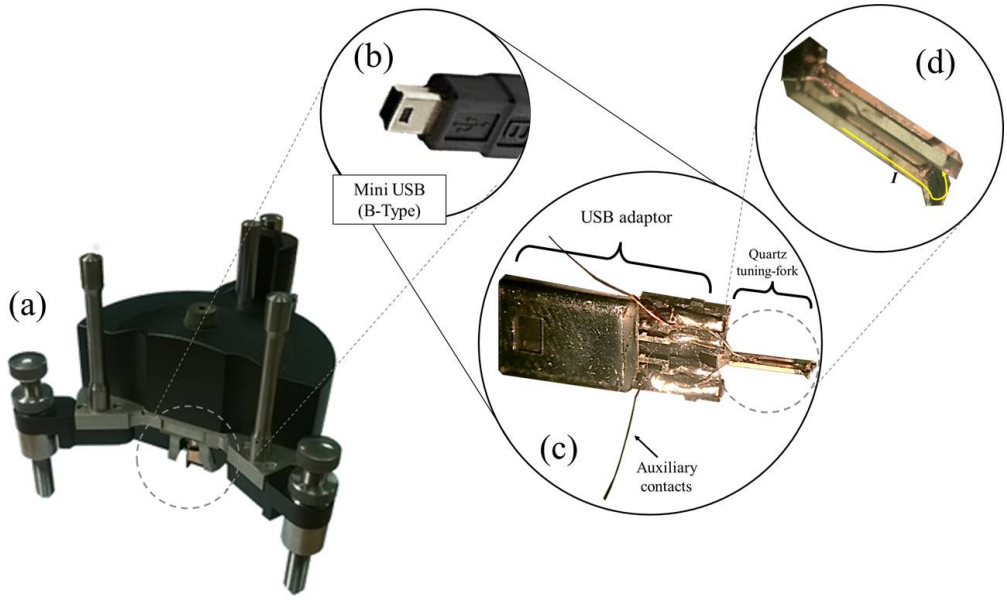

Figure 4.3: Implementation of the tuning fork (d) in the AFM setup. First the tuning fork is attached to an adapter (c) which consists of a Mini USB Type C plug (b), that can be connected to the AFM head (a).

This AFM head will perform the AFM operation and is therefore connected to the computation mechanisms. Using SPM software (Nova Px 3.4.0, NT-MDT) this head can be both monitored and controlled. In order to perform high quality imaging, it is essential that using this software all relevant parameters are adjusted in order to optimize the tip-sample interaction. The most important parameters are the **SetAmp** (amplitude of the oscillation), **Gen1Freq** (frequency of the oscillation), **Gen1Amp** (range of allowed amplitudes), **Gain** (the response intensity) and **Rate** (scan velocity).

Figure 4.4: NT-MDT NTEGRA AFM setup including vacuum setup.

At first the resonance frequency f_0 of the fork is determined by performing a frequency sweep. This sweep results in a frequency spectrum, from which besides f_0 also the Q factor can be retrieved using eqn. 2.6. Next, the tip is brought close to the sample and the other parameters are adjusted such that there is created a stable tip configuration. The system is now ready to operate.

Chapter 5

Results and Discussion

In this project the FPP is implemented in a TF-AFM setup, in order to perform high resolution surface characterization and thermal surface manipulation. This implementation induced certain challenges, which have to be resolved before the setup will operate properly. Firstly, the asymmetry induced by the FPP has to be resolved. When this procedure has optimized the sensitivity of the fork, the resolution of the setup will have to be improved in order to reach results similar to cantilever based AFM measurements, using vacuum setups. Finally, the thermomechanical patterning capabilities of the FPP will be examined in these vacuum conditions.

As discussed in the previous chapter, the attachment of the FPP to the tuning fork will cause an inbalance in the system, which needs to be rebalanced in order to optimize the sensitivity of the setup. The mass difference Δm between the upper and lower prong will adapted by shortening the lower prong. The difference in Q as a function of Δm is shown in fig. 5.1.

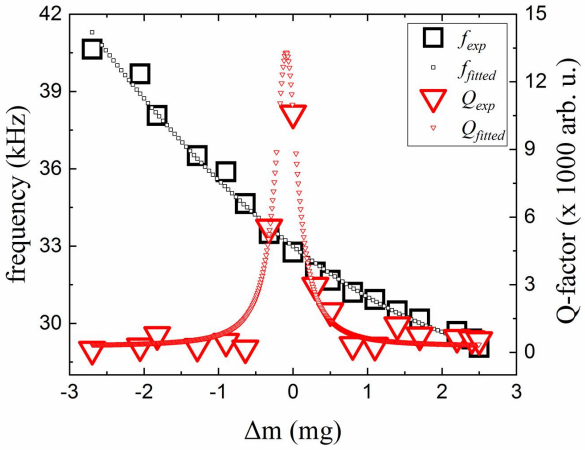

Figure 5.1: Influence on the extra load on the lower prong of the tuning fork on oscillation and sensitivity characteristics. On the left axes the resonance frequency (black), on the right axis the Q factor (red).

These experimental data obtained by Çiftçi in [37] confirm the findings of Rychen in his study [33]. According to the data, the mass difference Δm should be minimized to zero in order to achieve a Q factor as high as possible.

Therefore the length of the lower prong (L_1) of the tuning fork (fig. 5.2a) is reduced by gently polishing the TF (fig. 5.2b) in such a way that a zero mass difference is achieved when the FPP is attached (fig. 5.2c).

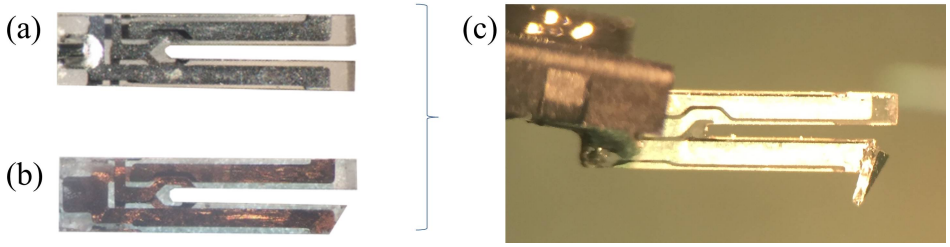

Figure 5.2: Rebalancing of the tuning fork, with the FPP attached to the TF before (a) and after the adjustment (b).

5.1 FPP Sensitivity

The tuning fork in fig. 5.2b is integrated in the experimental setup as discussed in section 4.2. To determine the Q factor of this tuning fork, a frequency sweep is performed by defining the resonance by measuring the piezo current I. The noise signal is in the order of 100 to 150 pA. The obtained spectrum show one high resonance peak around 33.00 kHz, which as a height of approximately 30 nA, which is approximately two orders larger than the noise signal. By enlarging this peak and performing another frequency sweep, the resonance frequency can be located with a precision of 0.5 Hz. During these sweeps, the software will automatically calculate the Q factor from eqn. 2.6.

Two results of this procedure are shown in fig. 5.3, where in fig. 5.3a a sweep is performed in ambient conditions and in fig. 5.3b vacuum effects are investigated.

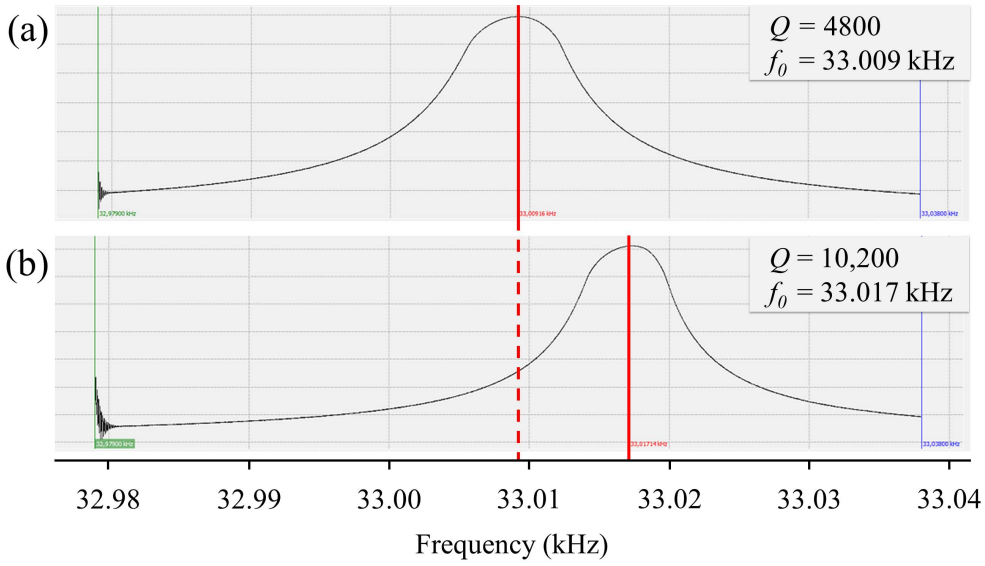

Figure 5.3: Results from the frequency sweep procedures in ambient (a) and vacuum (b) conditions. In the right top corner of both figures the found resonance frequency f_0 and the calculated Q factor are shown.

The first observable change between the ambient and vacuuum measurement is the shift in resonance frequency. In vacuum f_0 has a value that is 8 Hz higher than f_0 in ambient. This follows the expectation, as in vacuum the oscillator will experience less resistance from air particles and therefore which therefore results in a slightly higher f_0.

The other, much more important, change between the measurements in ambient and vacuum systems is the change in Q factor. In the measurement in fig. 5.3 the Q factor is more than doubled, to values exceeding 10^4. In order to obtain more reliable results, multiple measurements have been performed determining Q values in both conditions, of which the results are shown in table 5.1.

Table 5.1: Average Q factor in ambient and vacuum conditions.

	Average Q (10^3)
Ambient conditions	3.8 ± 0.6
Vacuum conditions	9.3 ± 0.4

As discussed in section 2.1.3, in order to obtain atomic resolutions comparable to cantilever based AFM it is required that the Q values are in the order of 10^4. From table 5.1 it can be concluded that vacuum measurements can reach Q values very close to 10^4, which will be sufficient for high resolution imaging using the FPP. Therefore, from now on all measurements in this project will be performed under vacuum conditions.

Once the resonance frequency of the tip f_0 has been locked by the software, the tip is brought in position several nanometers above the sample. At this point all parameters as discussed in section 4.2 will be optimized in order to create the most stabilized configuration. When a measurement is initialized, often one of this two major complications caused the measurement to fail:

– **The tip resonates at a frequency different from it's resonance frequency.**

  Often this is caused by external electromagnetic radiation which causes the tip to resonate at a different frequency. This will also affect the amplitude of the oscillation, resulting in unregulated oscillations which are easily observable in the result (fig. 5.4a). To resolve this, either the generated amplitude of the oscillation can be decreased or another tip-sample distance can be chosen, in order to avoid the external resonance.

– **The tip gradually withdraws from the sample, losing ability to scan properly.**

  When this happens, a steep increment is visible in the figure (fig. 5.4b). Usually this when this occurs, the generated amplitude or the gain is too low.

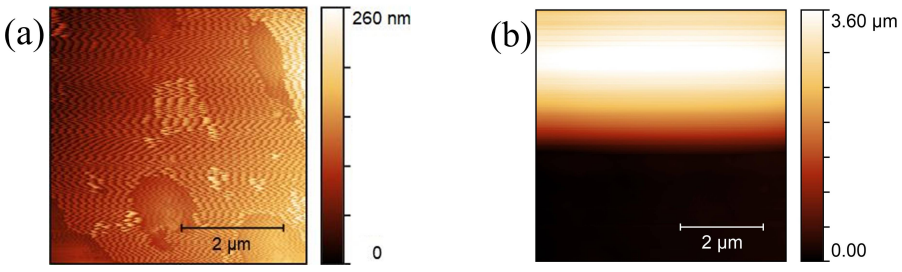

Figure 5.4: Possible complications during measurements, off-resonating behaviour of the tip (a) and withdraw of the tip (b).

5.2 FPP-based AFM imaging

Resolving this problems in order to obtain clear images is not very complicated, but mostly time consuming as an average AFM measurement takes 4 to 12 hours (depending on the initial conditions). The strategy is based on trial-end-error, which after many failure measurements leads to the optimal parameter configuration, which can differ for different TF. Using this set of parameters, it is possible to start perform high resolution AFM imaging. The first successful 5×5 µm AFM image in this project is obtained at a resonance frequency $f_0 = 33.01747$ kHz resulting in a quality factor $Q = 9.8 \times 10^3$. The optimal parameter configuration which led to the first success measurement is given in table 5.2.

Table 5.2: Parameters used in the first success measurement.

Parameter	Value
SetAmp	9.500 nA
Gen1Amp	0.3422
Gen1Freq	33.01747 kHz
Gain	0.120
Rate	0.0240 Hz
Resolution	1024×1024 px

The results are shown in fig. 5.5a. To determine the resolution of the image, plots are taken from enlargements of the AFM image (fig. 5.5b, 5.5d) in order to obtain the height characteristics in fig. 5.5c and 5.5e). The width of surface features in these height characteristics will define the resolution of the image. Therefore, the FWHM (full width at half maximum) of each peak is obtained by performing a Gaussian fit, which can be described by

$$f(x) = z_0 + A \exp\left\{-\frac{(x - x_0)^2}{2\sigma^2}\right\}. \tag{5.1}$$

From fitting the parameters z_0 (constant offset), A (height of the curve), x_c (center of the peak) and σ (standard deviation of the distribution), the FWHM can be retrieved from σ as

$$\text{FWHM} = 2\sqrt{2 \ln 2}\, \sigma \approx 2.35482\, \sigma. \tag{5.2}$$

The found values for the FWHM are also displayed in fig. 5.5c and 5.5e.

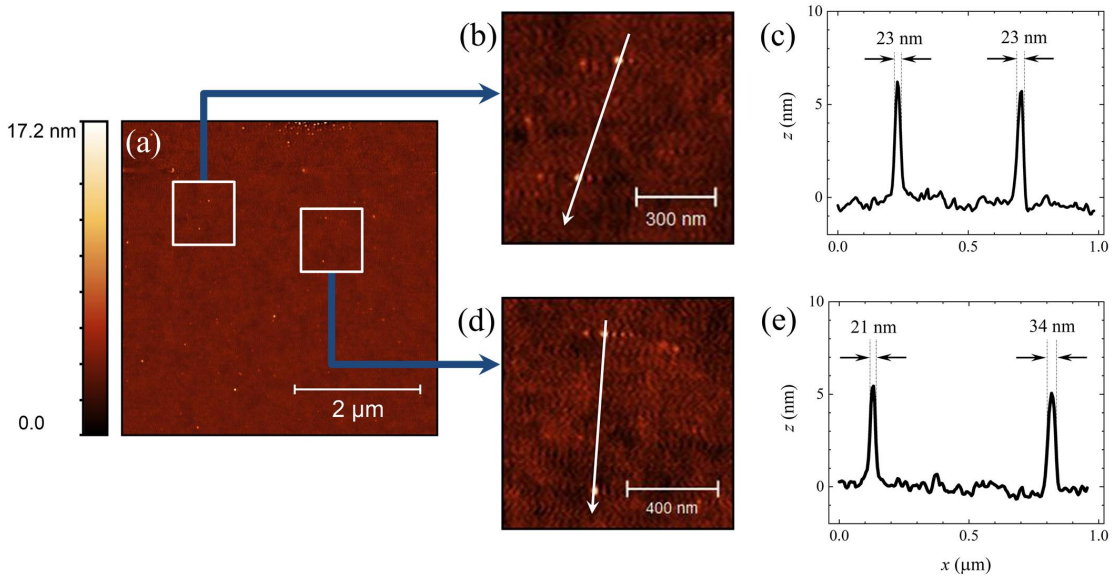

Figure 5.5: A 5×5 µm AFM image from a medium concentration paraffin sample in (a), which is enlarged in (b) and (d). The height characteristics along the arrows in these enlargements are shown in (c) and (e), showing the FWHM of the present peaks.

The results in fig. 5.5c show in two peaks, of 23.4 ± 0.5 nm (left) and 23.4 ± 2.5 nm (right). This result already shows that it is possible to reach resolutions down to 23.4 ± 2.5 nanometers, but the result from fig. 5.5e is even more interesting. In this figure the peaks are characterized by 21.4 ± 1.3 nm (left) and 34.4 ± 2.7 nm (right). The resolution can be defined by the difference of both values, resulting a resolution of 13.0 ± 3.0 nm. Again the results in fig. 5.6c and 5.6d will be anaylized by fitting the peaks by a Gaussian as described in eqn. 5.1 in order to determine the FWHM.

In order to confirm this result, another measurement is performed at a smaller scale (3×3 µm). As already thermal effects are investigated in this period, a different tuning fork is used in this measurement. This tuning fork was slightly smaller than the one used in the last measurement, which therefore results in a slighly lower Q. The TF has a resonance frequency of 32.61337 kHz resulting in $Q = 6.2 \times 10^3$. This is probably also the reason that higher currents are required through the TF in order to achieve similar oscillation amplitudes. The used current value is shown in table 5.3, together with all other relevant parameters. This configuration leads to the results shown in fig. 5.6.

Table 5.3: Parameters used in the second measurement.

Parameter	Value
SetAmp	9.700 nA
Gen1Amp	0.1422×10
Gen1Freq	32.61337 kHz
Gain	0.140
Rate	0.0352 Hz
Resolution	2048×2048 px

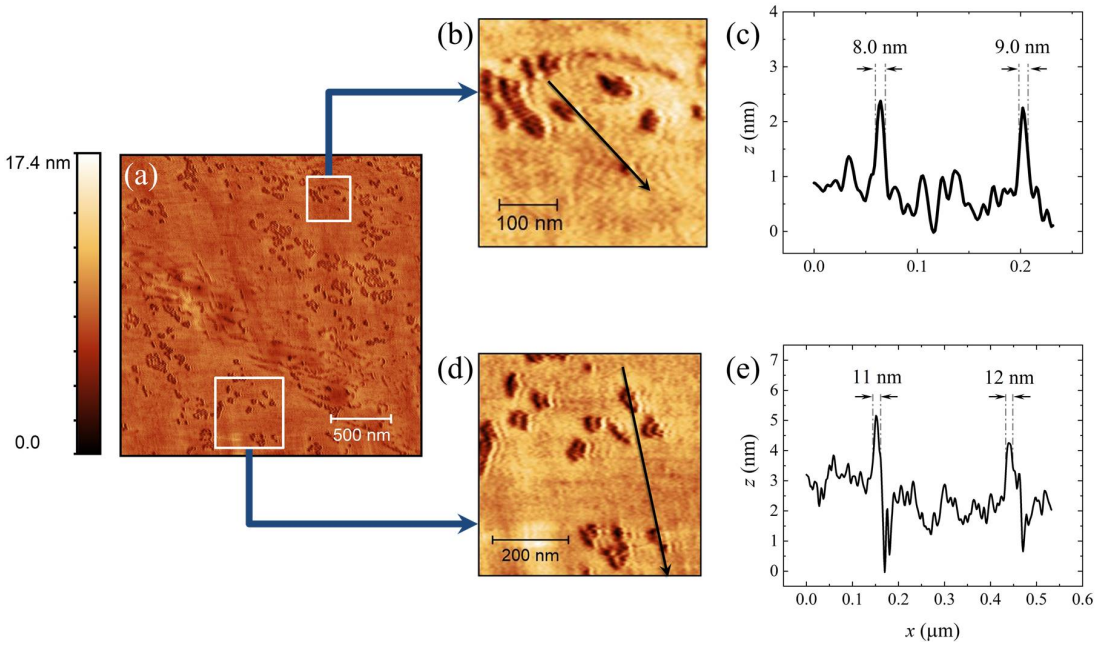

Figure 5.6: A 3×3 µm AFM image from a high concentration paraffin sample in (a), which is enlarged in (b),(d) of which the height characteristics are shown in (c),(e). In these figures the FWHM of the peaks is shown.

The topography in fig. 5.6c shows two peaks, characterized by FWHM values of 8.0 ± 0.6 nm (left) and 9.0 ± 0.4 nm. In fig. 5.6e, the peaks have FWHM values of 11.1 ± 0.9 nm (left) and 12.4 ± 2.3 nm (right). These results confirm the findings in fig. 5.5, that the FPP-assisted AFM is able to characterize on nanometer scales comparable to conventional setups.

5.3 FPP Induced thermomechanical modification

As the high resolution characterization abilities of the FPP have been proven, the next challenge is test the FPP on it's capability of surface manipulation. This is performed using the Keithley, as discussed in section 4.2. After producing a reference measurement, the tip can be brought in the desired position, after which the Keithley can be used. As the FPP is still operating in vacuum conditions, it is not well defined whether estimated currents of I in the COMSOL model will have a visible effect, as this model has been run using ambient conditions.

At first, currents pulses of 5 mA are applied using the Keithley for time intervals $\Delta t = \{4, 5, 6\}$ s. After performing an AFM scan it turned out that neither of these adaptations resulted in a visible change in the surface structure. This can be the influence of the vacuum conditions on the tip-sample interaction. Due to the absence of air particles it will cost more energy to achieve heat dissipation from the tip to the surface. Therefore other measurements are performed at increasing current. At $I = \{8, 10\}$ mA the sample still did not show any adaptations, but at 15 mA the first change in surface structure becomes visible, which is shown in fig. 5.7. In fig. 5.7a the reference measurement of 3×3 µm is shown, gathered before the surface was adapted. Then a 3 second pulse of 15 mA is applied at exactly the centre of reference measurement, of which the result is shown in fig. 5.7b.

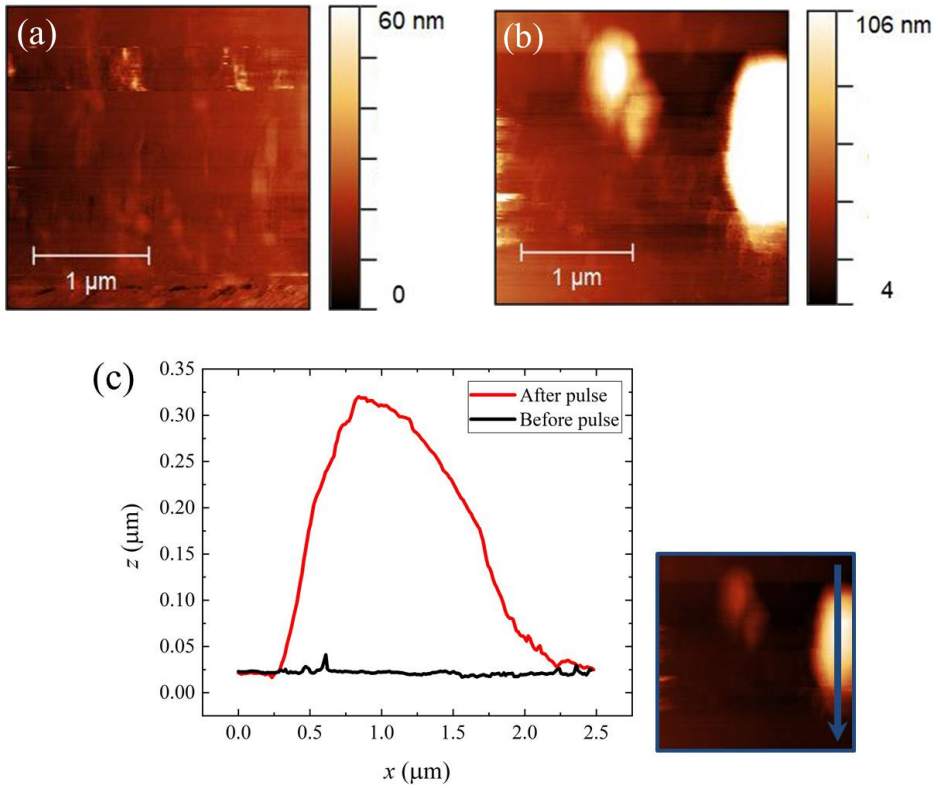

Figure 5.7: A 3×3 µm AFM image before (a) and afterwards a 3 s pulse of 15 mA at the centre of the measured surface (b). A cross section along the indicated arrow shows the topographic profile before and after the pulse (c).

In fig. 5.7b clearly the formation of a surface feature is visible, which has been elaborated in fig. 5.7c by performing a cross section through the features. The formation has a diameter of approximately 2 µm and a height of approximately 0.3 µm. This proves that the FPP is able to perform surface manipulation in vacuum conditions.

Chapter 6

Conclusions

In this project a new approach of thermomechanical patterning is investigated, based on FPP-assisted TF-AFM. During this investigation the imaging quality of this approach is examined using vacuum conditions and the AFM-assisted functionalization is tested under these same conditions.

In order to reach high resolution TF-AFM imaging comparable to cantilever based AFM, the requirement was to reach Q values in the order of 10^4. In order to reach this value using tuning fork techniques, measurements were performed under vacuum conditions to decrease any resistance from air particles. Frequency measurements on the tuning fork showed that the average Q factor in vacuum was equal to $(9.3 \pm 0.4) \times 10^3$, as the Q factor in ambient conditions took values of $(3.8 \pm 0.6) \times 10^3$. Vacuum measurements clearly are able to significantly increase the quality factor, and meet the requirement of $Q \simeq 10^4$. These vacuum measurements resulted in several high resolution images. In this project resolutions up to 8.0 ± 0.6 nm are achieved using AFM imaging. These scales clearly show that TF-AFM imaging in vacuum conditions is capable of achieving resolutions comparable to cantilever based imaging methods.

Besides imaging, also functionalization of the introduced functionalized planar probe (FPP) has been investigated under the same vacuum conditions. In these conditions it was harder to achieve thermal surface modifications than in ambient conditions, as more current was needed in order to obtain similar results. It is shown that thermomechanical surface modification is possible in vacuum condition, using a current of 15 mA, where 5 mA was sufficient in ambient conditions.

In further investigations regarding this project, more research has to be done on thermomechanical patterning in vacuum conditions, as in this project it only was possible to qualitatively thermal surface effects so far. It is necessary to do more quantitative measurements on surface features and also construct a COMSOL model for the FPP in vacuum conditions.

When this have been achieved, other materials than paraffin can be investigated, in order to show the abilities of this approach to operate on a wide spectrum of materials. It is challenging to investigate materials which have thermal properties very different from paraffin, which is relatively easy to adapt by thermal means.

Besides thermal effects, the FPP could also be investigated on magnetic manipulation. The current through the nanobridge at the tip-end of the FPP can generate a magnetic field (Oersted field) which can be used as a tool for manipulation of local magnetic surface properties.

Bibliography

[1] F. Braet and M. Radmacher, "Foreword to the special issue on afm in biology & bionanomedicine," *Micron*, vol. 43, no. 12, p. 1211, 2012. Special issue on AFM in Biology & Bionanomedicine. 1

[2] M. Endo, "AFM-based single-molecule observation of the conformational changes of DNA structures," *Methods*, 2019. 1

[3] T. Uchihashi, H. Watanabe, S. Fukuda, M. Shibata, and T. Ando, "Functional extension of high-speed AFM for wider biological applications," *Ultramicroscopy*, vol. 160, pp. 182 – 196, 2016. 1

[4] R. Wiesendanger and W. Roland, *Scanning Probe Microscopy and Spectroscopy: Methods and Applications*. Scanning Probe Microscopy and Spectroscopy: Methods and Applications, Cambridge University Press, 1994. 3

[5] G. Binnig, C. F. Quate, and C. Gerber, "Atomic force microscope," *Physical review letters*, vol. 56, no. 9, p. 930, 1986. 3

[6] NT-MDT Spectrum Industries, "Scan Page," 2018. 3

[7] B. Bhushan, *Springer Handbook of Nanotechnology*. Springer Handbooks, Springer Berlin Heidelberg, 2017. 4

[8] B. Bhushan, *Handbook of Micro/Nano Tribology*. CRC press, 1998. 4

[9] S. Rützel, S. I. Lee, and A. Raman, "Nonlinear dynamics of atomic–force–microscope probes driven in lennard–jones potentials," *Proceedings of the Royal Society of London. Series A: Mathematical, Physical and Engineering Sciences*, vol. 459, no. 2036, pp. 1925–1948, 2003. 4

[10] S. Magonov, V. Elings, and M.-H. Whangbo, "Phase imaging and stiffness in tapping-mode atomic force microscopy," *Surface Science*, vol. 375, no. 2, pp. L385 – L391, 1997. 5, 9

[11] H. Hölscher, *AFM, Tapping Mode*, pp. 99–99. Dordrecht: Springer Netherlands, 2012. 5

[12] P. K. Hansma, J. P. Cleveland, M. Radmacher, D. A. Walters, P. E. Hillner, M. Bezanilla, M. Fritz, D. Vie, H. G. Hansma, C. B. Prater, J. Massie, L. Fukunaga, J. Gurley, and V. Elings, "Tapping mode atomic force microscopy in liquids," *Applied Physics Letters*, vol. 64, no. 13, pp. 1738–1740, 1994. 5

[13] M. Manning, "Eem. nanotechnology and nanoelectronics," 2016. 6

[14] H. Hölscher, *AFM, Non-contact Mode*, pp. 93–99. Dordrecht: Springer Netherlands, 2012. 6

[15] A. Checco, Y. Cai, O. Gang, and B. M. Ocko, "High resolution non-contact afm imaging of liquids condensed onto chemically nanopatterned surfaces," *Ultramicroscopy*, vol. 106, no. 8, pp. 703 – 708, 2006. Proceedings of the Seventh International Conference on Scanning Probe Microscopy, Sensors and Nanostructures. 6

[16] H. Edwards, L. Taylor, W. Duncan, and A. J. Melmed, "Fast, high-resolution atomic force microscopy using a quartz tuning fork as actuator and sensor," *Journal of applied physics*, vol. 82, no. 3, pp. 980–984, 1997. 6, 7, 10, 14

[17] M. Bao, "Chapter 2 - mechanics of beam and diaphragm structures," in *Analysis and Design Principles of MEMS Devices* (M. Bao, ed.), pp. 33 – 114, Amsterdam: Elsevier Science, 2005. 8

[18] W. M. Siebert, *Circuits, signals, and systems*, vol. 2. MIT press, 1986. 8

[19] J. H. Harlow, *Electric power transformer engineering*. CRC press, 2003. 8

[20] E. I. Green, "The story of Q," *American Scientist*, vol. 43, no. 4, pp. 584–594, 1955. 8

[21] F. J. Giessibl, F. Pielmeier, T. Eguchi, T. An, and Y. Hasegawa, "Comparison of force sensors for atomic force microscopy based on quartz tuning forks and length-extensional resonators," *Physical Review B*, vol. 84, no. 12, p. 125409, 2011. 10

[22] Y. Gan, H. Wong, and W. Lee, "A novel atomic force microscopy based lithography system for automated patterning via anodic oxidation," *Composites Part B: Engineering*, vol. 42, no. 3, pp. 456 – 461, 2011. 11

[23] Y. Wada, "Possible application of micromachine technology for nanometer lithography," *Microelectronics Journal*, vol. 29, no. 9, pp. 601 – 611, 1998. Low Dimensional Structures and Devices: Micromachined Devices. 11

[24] L. Ressier and V. L. Nader, "Electrostatic nanopatterning of PMMA by AFM charge writing for directed nano-assembly," *Nanotechnology*, vol. 19, p. 135301, feb 2008. 11

[25] Z. Davis, G. Abadal, O. Hansen, X. Borisé, N. Barniol, F. Pérez-Murano, and A. Boisen, "AFM lithography of aluminum for fabrication of nanomechanical systems," *Ultramicroscopy*, vol. 97, no. 1, pp. 467 – 472, 2003. Proceedings of the Fourth International Conference on Scanning Probe Microscopy, Sensors and Nanostructures. 11

[26] S. F. Lyuksyutov, R. A. Vaia, P. B. Paramonov, S. Juhl, L. Waterhouse, R. M. Ralich, G. Sigalov, and E. Sancaktar, "Electrostatic nanolithography in polymers using atomic force microscopy," *Nature Materials*, vol. 2, no. 7, p. 468, 2003. 11

[27] S. F. Lyuksyutov, P. B. Paramonov, S. Juhl, and R. A. Vaia, "Amplitude-modulated electrostatic nanolithography in polymers based on atomic force microscopy," *Applied physics letters*, vol. 83, no. 21, pp. 4405–4407, 2003. 11

[28] S. F. Lyuksyutov, P. B. Paramonov, R. A. Sharipov, and G. Sigalov, "Induced nanoscale deformations in polymers using atomic force microscopy," *Physical Review B*, vol. 70, no. 17, p. 174110, 2004. 11

[29] P. Vettiger, M. Despont, U. Drechsler, U. Durig, W. Haberle, M. I. Lutwyche, H. E. Rothuizen, R. Stutz, R. Widmer, and G. K. Binnig, "The Millipede - More than thousand tips for future AFM storage," *IBM Journal of Research and Development*, vol. 44, no. 3, pp. 323–340, 2000. 12

[30] Y. Fang, Y. Ni, S.-Y. Leo, C. Taylor, V. Basile, and P. Jiang, "Reconfigurable photonic crystals enabled by pressure-responsive shape-memory polymers," *Nature communications*, vol. 6, p. 7416, 2015. 12

[31] T. Siahaan, O. Kurnosikov, B. Barcones, H. Swagten, and B. Koopmans, "Cleaved thin-film probes for scanning tunneling microscopy," *Nanotechnology*, vol. 27, no. 3, p. 03LT01, 2015. 14, 17

[32] Y.-J. Chen, A. Huang, T. Ellingham, C. Chung, and L.-S. Turng, "Mechanical properties

and thermal characteristics of poly (lactic acid) and paraffin wax blends prepared by conventional melt compounding and sub-critical gas-assisted processing (SGAP)," *European Polymer Journal*, vol. 98, pp. 262–272, 2018. 15

[33] J. Rychen, *Combined low-temperature scanning probe microscopy and magneto-transport experiments for the local investigation of mesoscopic systems*. PhD thesis, ETH Zurich, 2001. 16, 18, 21

[34] A. Castellanos-Gomez, N. Agraït, and G. Rubio-Bollinger, "Dynamics of quartz tuning fork force sensors used in scanning probe microscopy," *Nanotechnology*, vol. 20, no. 21, p. 215502, 2009. 16

[35] L. González, R. Oria, L. Botaya, M. Puig-Vidal, and J. Otero, "Determination of the static spring constant of electrically-driven quartz tuning forks with two freely oscillating prongs," *Nanotechnology*, vol. 26, no. 5, p. 055501, 2015. 16

[36] T. R. Albrecht, P. Grütter, D. Horne, and D. Rugar, "Frequency modulation detection using high-q cantilevers for enhanced force microscope sensitivity," *Journal of Applied Physics*, vol. 69, no. 2, pp. 668–673, 1991. 16

[37] H. Tunç Çiftçi, Laurent Pham Van, Bert Koopmans, Oleg Kurnosikov, "AFM-assisted polymer patterning with functionalized planar probes." 2019. 17, 21

Appendix A

Experimental Manual

In this appendix the experimental methods used in this project will be discussed. These methods can be divided into two different categories: surface characterization and surface modification.

A.1 AFM Characterization

The surface characterization is performed using an NT-MDT NTEGRA AFM head, SNLG113USB model. The data that is provided by this AFM head is interpreted by a computational setup connected to a desktop computer, running NT-MDT software (Nova_Px_3.4). This software is able to sent information to the AFM head and can retrieve scanning data from this AFM head.

In order to start a scanning measurement, the following steps have to be taken:

- It is essential that in the initial state the tip is withdrawn from the sample ($D \gg 10$ nm). The measured tip-sample distance D is monitored in the colour indicated meter on top of the page (fig. A.1a). When D is measured large, the meter is filled and colours blue. In the optimal configuration the meter colours green. When the meter colours red, the tip-sample distance is (critically) low and action should be taken in order to prevent a tip-sample crash.
- As discussed, the tip-sample distance is correlated to the amplitude of the oscillation of the probe. It therefore is essential to choose proper values of the set and target amplitude. These values can be found in the *resonance* window. In fig. A.1 the target amplitude (**SetPoint**) is set in (c) and the initial set amplitude (**Gen1Amp**) in (b) can be adjusted such that it reaches the SetPoint. The closer the Gen1Amp reaches the SetPoint, the more sensitive the setup will operate, but when the Gen1Amp is lower than the SetPoint, the setup will not be able to perform measurements. Therefore it is essential that **Gen1Amp** > **SetPoint**. During measurements the SetPoint often is set to 9.5 nA, while the Gen1Amp is set between 10.0 and 10.5 nA.
- In the same *resonance* window then the resonance frequency of the fork is found by performing a **frequency sweep**. This sweep is performed over 10,000 points between two manually adjusted boundaries. The resonance frequency f_0 is found at a sharp peak in the spectrum, and in order to correct this value, the boundaries can be adjusted to span a smaller frequency range. Now the resonance frequency can be set more precise. This procedure can be repeated several times until no improvements are observable anymore.

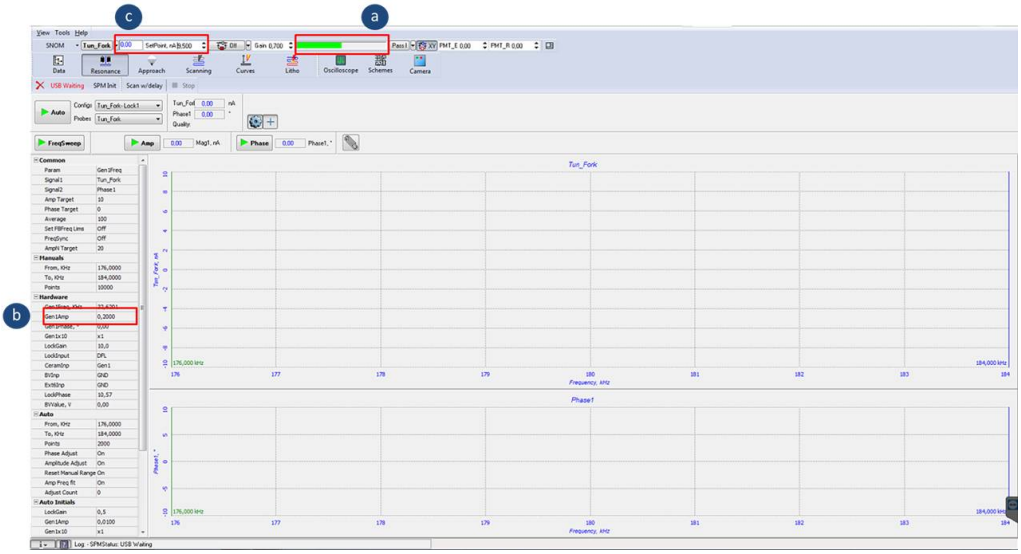

Figure A.1: Resonance window of the NT-MDT Nova_Px software

– At this point the "landing" of the probe can be started, which is done in the *approach* window. The rate at which the probe is approaching the sample is adjustable and during these measurements set at 1.75 nm s^{-1}. Before the landing has been started, the measured surface height will be constant at $z = 0$ nm. When the probe has landed, the height will increase to a constant value of approximately 4 to 6 nm.

– Now it is observable whether the tip is under influence of external resonance, when large amplitude oscillations are visible. This can be resolved by lowering the Set1Amp, or choosing a different SetPoint.

– The setup is now ready to perform measurements. In the *scanning* window, all relevant parameters can be configured, such as the **scan rate**, **scan area** and **scan angle**.

– When everything is configured, in the window will appear how long the measurement will take. The measurement will start as soon as the "run" button is pressed.

A.2 AFM Surface Modification

Surface modification achieved using a FPP is based on an electric current that is confined at the tip-end, as discussed in section 2.2.1. This electric current is generated by a Keithley instrument. In the setup a Keithley 2400 is used, which can serve as both a highly stable DC power source and true instrument grade 6.5 digit multimeter.

In this project the power source properties of this instrument are used in order to apply currents through the FPP. For this project specific current pulses are applied for several seconds. The procedure is as follows:

- First, the Keithley is set in current pulse mode. After starting the instrument by pressing **START**, the Keithley is put in current source mode by pressing **EDIT** and **I** afterwards. In order to create a pulse, **CONFIG** and **SWEEP** are selected, after which the type of pulse can be specified.
- In this project only rectangular pulses are used. In order to configure the Keithley in this way, **TYPE** and after this **CUSTOMSWEEP** are selected. By selecting **# Points**, the number of points can be specified, which in this case should be adapted to 2. The amplitude of the pulse can be adjusted by selecting **ADJUST POINTS**. At point 0, the value for the current should be adjusted to the desired pulse intensity. At point 1, the value should return back to 0. To adjust to pulse width, return back to the main screen and select **CONFIG** and press **I**. The desired pulse with can be set after selecting **DELAY**.
- The pulse is applied by pressing the **ON/OFF** button.

Figure A.2: Front view of a Keithley 2400 current generator